Journal of Polymer Research (2021) 28: 419
https://doi.org/10.1007/s10965-021-02786-6

ORIGINAL PAPER

Physico-chemical and piezoelectric characterization of electroactive nanofabrics based on functionalized graphene/talc nanolayers/PVDF for energy harvesting

Sawan Shetty[1] · A. M. Shanmugharaj[2] · S. Anandhan[1]

Received: 7 August 2021 / Accepted: 3 October 2021 / Published online: 11 October 2021
© The Polymer Society, Taipei 2021

Abstract
Poly(vinylidene fluoride) (PVDF) is a versatile polymer, whose dielectric, piezoelectric and ferroelectric properties can be augmented by a range of processing routes and/or additives. We developed a flexible nanogenerator using electrospun PVDF/COOH-functionalized graphene nanosheet (FGNS)/talc nanosheet (TNS) hybrid nanocomposites. TNS loading was fixed at 0.50 wt% while FGNS loading was varied (0.05, 0.10, 0.15, and 0.20 wt %) in these nanofabrics and their structure–property relationship was explored. Incorporation of FGNS led to formation of an electrically conductive network in the polymer matrix aided by TNS and electrospinning. The uniform dispersion of the filler nanosheets led to effective enhancement of the electroactive β-phase of the PVDF matrix. Crystallinity and polymorphism in these systems were explored by FTIR spectroscopy, X-ray diffraction and differential scanning calorimetry. A nanogenerator made of the nanofabric containing 0.5 wt% of TNS and 0.10 wt% of FGNS was mechanically impacted by pneumatic actuator (operating pressure 0.4 MPa), resulting in an output voltage of 12.9 V and a power density of 1.72 μW/cm^2, respectively. The piezoelectric coefficient (d_{33}) of this nanofiber system was 61 pm/V as revealed by piezoelectric force microscopy. These novel nanocomposites could be used in flexible energy-harvesting devices.

Keywords Poly(vinylidene fluoride) · Electrospinning · Energy · Nanogenerator · Piezoelectric

Introduction

Rapid advancement in the internet of things has seen an upsurge in the development of microelectronic devices that is crucial for the performance of the former. These microelectronic devices require relatively low power for their operation in the range of nano-watts to milli-watts [1]. Powering these microelectronic devices via a piezoelectric energy harvesting source has gained momentum as the latter delivers uninterrupted power supply to the former, thereby making them self-powered [2, 3]. In this direction, poly(vinylidene fluoride) (PVDF) with its piezoelectric, ferroelectric, pyroelectric, and flexible characteristics has been a potential choice of material for developing self-powered flexible microelectronic devices [4]. Among the polymorphic phases of PVDF, the electroactive β- and γ-phases are accountable for its piezoelectric response. The β-phase has fluorine and hydrogen atoms arranged on either side of the polymer backbone, i.e., all-trans (TTTT) chain conformation, resulting in a significant dipole moment compared to the γ-phase [5, 6]. Thus it necessitates promoting the β-phase to enhance the piezoelectric response of PVDF. Further, the piezoelectric coefficient of PVDF is relatively lesser than its piezoelectric ceramic counterparts. Hence, methods such as forming composites, mechanical stretching, and electrical poling are adopted to enhance the piezoelectric response of PVDF and its functional applicability [7–10].

Electrospinning is an efficient technique favoring the formation of electroactive β-phase of PVDF. During electrospinning, the PVDF nanofibers experience a mechanical stretching/electrical poling effect due to the elongation and whipping of the polymer jet that further contributes to

✉ S. Anandhan
anandtmg@gmail.com; anandhan@nitk.edu.in

[1] Department of Metallurgical and Materials Engineering, National Institute of Technology Karnataka, Surathkal, Mangaluru 575025, India

[2] Centre for Energy and Alternative Fuels/Department of Chemistry, Vels Institute of Science, Technology & Advanced Studies (VISTAS), Tamil Nadu, Chennai 600 117, India

the enhancement of the electroactive phase of the latter. Previously reported articles demonstrated the transition of the α- phase to the β-phase of PVDF via electrospinning [11–15]. Further, the inclusion of nanosize fillers/additives has enhanced the piezoelectric property of PVDF by providing nucleation sites for the growth and promotion of β-crystallites [16–20]. For example, Neppalli et al. reported that clay and electrospinning synergistically promoted the β-phase of PVDF/clay composite [21]. The authors proposed that: clay functioned as both nucleating agent and hindrance to polymer chain mobility while electrospinning aided the elongation of the polymer chain, thereby facilitating the all-trans conformation of PVDF. Liu et al. proposed an ion–dipole interaction between organically modified montmorillonite (OMMT) and PVDF that led to the stabilization of polar phases (β-/γ-phase) with the elimination of α-phase in the electrospun PVDF/OMMT composites [22]. Thus clay mineral fillers have been a popular choice to induce polar crystalline phases in the PVDF matrix. On the other hand, carbon-based fillers have also been successful in tuning the electroactive phases of PVDF [23, 24]. Among them, graphene has been a potential filler in polymer matrices owing to its high surface area, dominant aspect ratio, flexibility, and enhanced mechanical, thermal, and electrical properties [25, 26]. Abolhasni et al. reported the fabrication of PVDF/graphene composite nanofiber by electrospinning [27]. Their results indicated that the inclusion of 0.1 wt% of graphene in the PVDF matrix significantly enhanced the electroactive β-phase fraction that subsequently led to the higher piezoelectric response of the composite nanofibers. Agglomeration/aggregation is inevitable in graphene-based fillers. Hence, functionalization of graphene is a prerequisite that aids its dispersion in a polymer matrix, following an improved adhesion and interfacial interaction with the host matrix. Recently, Ongun et al. synthesized graphene oxide (GO) and reduced graphene oxide (RGO) by Hummer's method and incorporated them into PVDF matrix by electrospinning process [28]. The PVDF/RGO based composite with a loading of 0.8wt% of RGO resulted in a four-fold increment in open-circuit voltage value compared to pristine PVDF nanofibers. The authors ascribed the improved piezoelectric response of the composite to strong interactions between PVDF and RGO. In our recent work, a low loading of 0.50 wt% talc nanosheet in the PVDF matrix was able to enhance the nanocomposite fabric's piezoelectric response significantly. The authors ascribed this to the high-aspect ratio of the talc nanosheets along with their strong interactions with the polymer matrix via hydrogen bonds [29]. However, the piezoelectric response of the PVDF composite nanofabrics was comparable but not higher than that of most of the carbon-based fillers (CNT, graphene)/PVDF composites. Hence, the current work's motivation was to further improve the performance of talc nanosheets/PVDF composite nanofabrics by the inclusion of carboxyl functionalized graphene nanosheets. Lately, a hybrid combination of fillers, such as silver/RGO, barium titanate/graphene, calcium carbonate/MMT, has effectively enhanced the electroactive phases of PVDF [30–32].

Thus, in this work, new flexible electroactive nanofabrics with superior piezoelectric property were electrospun from PVDF/carboxyl functionalized graphene nanosheet (FGNS)/talc nanosheet (TNS) hybrid nanocomposite. In these hybrid nanocomposite nanofabrics (TGP), TNS loading was fixed at 0.50 wt%, and FGNS loading was varied (0.05, 0.10, 0.15, and 0.20 wt%) relative to PVDF. Herein, functionalization of graphene nanosheets improved the compatibility with the polymer matrix, and the carboxyl groups of FGNS were anticipated to promote the β-phase of PVDF via interfacial interactions. Further, FGNS could provide electrically conducting pathway for the easy alignment of β-phase PVDF. Apart from its interfacial interactions with PVDF, TNS was also anticipated to enhance the dispersibility of FGNS thereby an electrically conductive network formation in the PVDF matrix [33, 34]. Piezoelectric performance of a nanogenerator assembled from these hybrid nanocomposite nanofabrics was evaluated using piezoelectric response force microscopy (PFM) and a custom-made pneumatic compression setup.

Experimental details

Materials

Natural graphite flakes, sodium nitrate, potassium permanganate, hydrogen peroxide, sulphuric acid, hydrochloric acid, para-aminobenzoic acid were procured from Sigma Aldrich, Korea. PVDF ($\overline{M_W}$=575,000, Solef 1051, Belgium) was purchased from Prakash Chemicals Pvt.Ltd, Vadodara, India. Talc nanoparticles (Celina-80, Nanoshell, USA, purity: 99.9%, avg. particle size: < 100 nm) were procured from Intelligent Materials Pvt. Ltd, Punjab, India. *N, N'*-dimethylformamide (DMF) and acetone were purchased from Molychem, India. All the chemicals used were of analytical grade.

Preparation of graphene oxide (GO) and reduced graphene oxide (RGO)

GO was prepared from purified natural graphite according to modified Hummer's method [35, 36]. Typically, 1 g of graphite flakes was dispersed in 100 mL of sulphuric acid by sonication for 30 min, followed by addition of 1 g of sodium nitrate. To the resultant mixture, 6 g of potassium permanganate was gently added under the ice-cold condition. This mixture was stirred for 2 h maintaining the water

bath temperature at 35 °C. Next, 40 mL of de-ionized water (70 °C) was added drop-wise to the solution, and the temperature of the solution was elevated to 90 °C. At last, 140 mL of de-ionized water (70 °C) followed by 20 mL of hydrogen peroxide (30 wt%) was added so as to terminate the reaction. The as-prepared GO dispersion was purified via the dialysis route to remove any residual salts and acids. Finally, the resultant GO was dried overnight in a vacuum oven at 60 °C. For the preparation of RGO, above synthesized GO was subjected to a temperature of 400 °C in a muffle furnace under a nitrogen atmosphere for 3 h [37].

Synthesis of carboxyl functionalized graphene nanosheets (FGNS)

The chemical functionalization of RGO was done via a diazonium coupling reaction using aminobenzoic acid [38]. Briefly, 960 mg of para-aminobenzoic acid was added to 80 mL deionized water. To this solution, 526 mg (7.6 mmol) sodium nitrate was introduced slowly via a dropper, while the solution was maintained in an ice bath and stirred till the solution became clear. Next, 6 mL HCl (20 v/v%) solution was quickly added and stirred for another 45 min till the solution turned yellow. The resultant diazonium salt solution was added to an aqueous solution of RGO (250 mg), maintained at 5 °C, and stirred for 6 h. After this, the reaction mixture was further stirred for 8 h under ambient conditions. Finally, the obtained products were filtered and washed repeatedly with de-ionized water and later dried overnight in vacuum at 60 °C to obtain FGNS. The schematic illustration of the synthesis method was displayed in Fig. 1.

Electrospinning of PVDF and TGP-based nanocomposite nanofabrics

For preparing electrospun PVDF nanofabrics (E-PVDF), PVDF powder (13.5 wt/v%) was dissolved in 9:1 v/v mixture of DMF/acetone and stirred for 10 h at 30 °C. For the TGP-based nanocomposite nanofabrics, desired amount of FGNS was first dispersed in the solvent mixture by ultrasonication for 1 h, and then TNS was added under stirring followed by ultrasonication for another 1 h. To the resultant mixture, PVDF powders were added followed by continuous magnetic stirring for 10 h to produce a homogeneous electrospinning solution. For the TGP-based system, talc nanosheets content was fixed at 0.50 wt% and FGNS loading was varied (0.05, 0.10, 0.15, and 0.20 wt%) relative to PVDF. The prepared electrospinning solution was then loaded into a 10 mL syringe with a stainless steel needle (22-G), and electrospinning

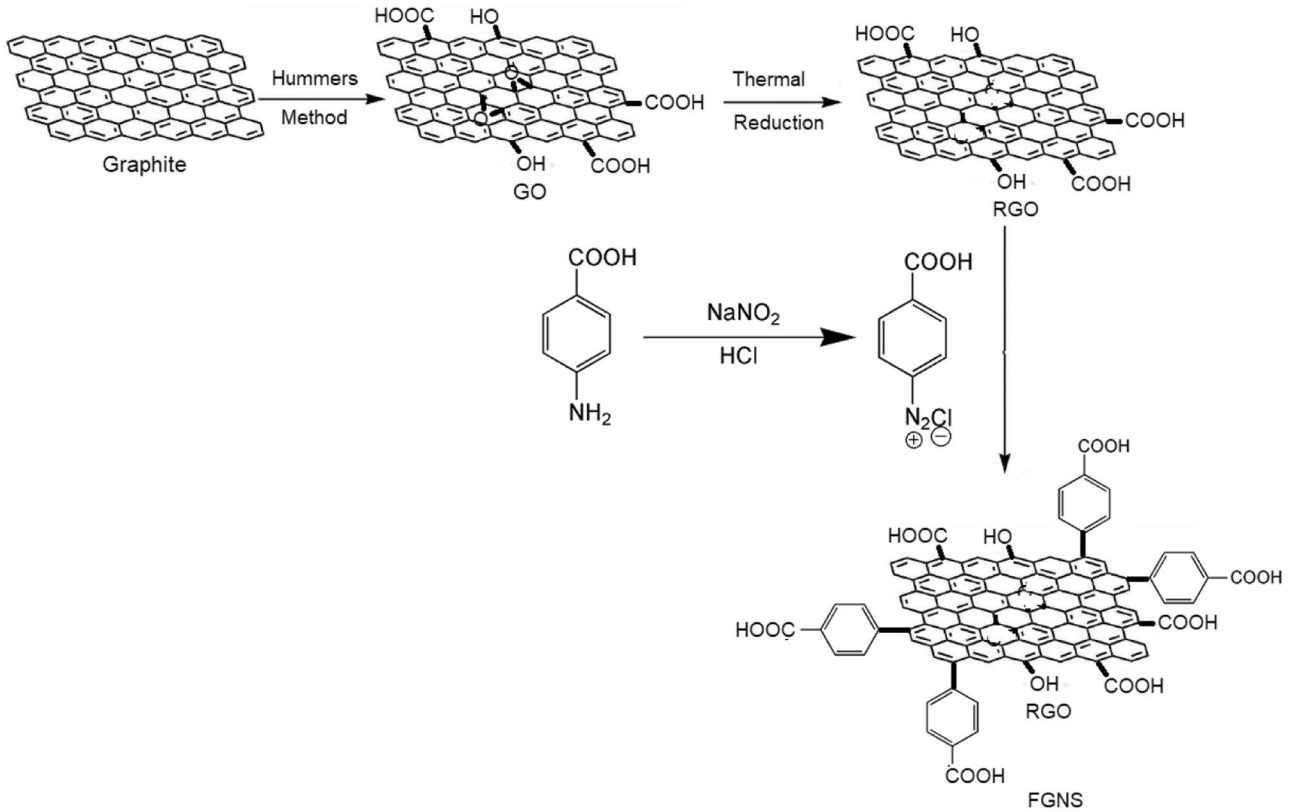

Fig. 1 Schematic depicting the synthesis of GO, RGO, and FGNS

was performed at 30 °C on a vertical electrospinning unit (Espin-NanoV1-Physics Equipments Co., India) under the following optimized conditions: voltage 18 kV; flow rate 0.6 mL/h; tip to collector distance 16 cm; rotating drum collector speed 1400 rpm; and relative humidity 52 ± 2%.

Characterization

The morphological features of the samples were examined by field emission scanning electron microscopy (FESEM) (ZEISS GeminiSEM-300, Germany). All the samples were deposited with thin layer of gold prior to FESEM observation. The surface elemental composition was measured using energy dispersive X-ray spectroscopy (EDS) (AMETEK-Elite Super, Japan). X-ray diffraction (XRD) of the samples was done using X-ray diffractometer (Empyrean-Malvern Panalytical, UK) with Cu K_α radiation ($\lambda = 0.154$ nm) under 45 kV and 30 mA. The morphology and structure of synthesized samples were further investigated using transmission electron microscopy (TEM) (JEOL-2100, Japan). Raman spectra were acquired using a Raman spectrometer (Horiba-LabRAM HR, France) using a 532 nm laser source. Fourier transform infrared spectroscopy (FTIR) (JASCO-4200, Japan) was performed in the wavenumber range of 4000 cm^{-1} – 400 cm^{-1} for nanoparticles (KBr mode) and 4000 cm^{-1} – 650 cm^{-1} for electrospun nanofabrics (ATR mode) with 32 accumulated scans at a resolution of 4 cm^{-1}. Differential scanning calorimetry (DSC) (PerkinElmer-6000, USA) was performed at a heating rate of 10 °C/min under dry nitrogen atmosphere at a temperature range of 0 to 200 °C. The mechanical properties of the electrospun nanofabrics (50 mm × 10 mm) were measured using a universal testing machine (INSTRON-5967, USA) at a crosshead speed of 5 mm/min. For the piezoelectric evaluation, a nanogenerator was assembled with the synthesized electrospun nanofabrics. The construction detail of the nanogenerator is described in Sect. S1, ESI. Later, the assembled nanogenerator was mechanically impacted by a custom-built pneumatic compression setup (FESTO-DSNU-20–100-P-A, Germany) operating at an inlet pressure of 0.4 MPa (Sect. S2, ESI). The corresponding output voltage was recorded on a USB oscilloscope (Digilent-Analog Discovery 2, USA). The local ferroelectric hysteresis loop and piezoelectric coefficient (d_{33}) of the electrospun nanofabrics were measured by piezoelectric force microscopy (PFM) (Asylum Research- MFP-3D-BIO, USA). The Ti/Ir coated tip (Asylum Research-ASYELEC-01, USA) with a spring constant of 2 N/m was used for the measurements. The hysteresis loop was analyzed under the dc bias voltage range of –30 V to + 30 V.

Results and discussion

Characterization of carboxyl functionalized graphene nanosheets (FGNS)

The FTIR spectra of GO, RGO, and FGNS are shown in Fig. 2. In the spectrum of GO, the absorption peaks at 3400 and1720 cm^{-1} correspond to the O−H stretching and carboxyl C = O stretching, respectively. Further, the absorption peaks at 1228 and 1045 cm^{-1} are assigned to the epoxy C−O stretching. The peak at 1620 cm^{-1} is assigned to the stretching and bending vibrations of adsorbed water molecules on the GO [39–42]. In the spectrum of RGO the absorption peak at 1720 cm^{-1} completely disappeared, and the intensity of peak at 1620 cm^{-1} is noticeably reduced. This implies a significant reduction in the oxygen functional groups of RGO. The FGNS exhibits strong absorptions at 1555 and 1171 cm^{-1} due to the C−C stretching and C−H bending vibrations related to the aromatic benzene groups [43]. And C-O stretching vibrations of -COOH group can also possibly appear in that range. The absorption peak at 1685 cm^{-1} is assigned to the C = O stretching of aromatic carboxylic acids. [44] The peak at 780 cm^{-1} is due to C−H out of plane bending vibrations in the benzene rings [45]. Moreover, the absence of a peak in the range of 2200–2300 cm^{-1} corresponding to the diazonium group's N≡N stretching mode corroborates the grafting mechanism of benzoate on the RGO [46].

XRD patterns of GO, RGO, and FGNS are shown in Fig. 3. Compared to the reference graphite diffraction pattern (ICDD-00–001-0646), GO displays a sharp peak at 9.41° (001) that corresponds to an interlayer space of

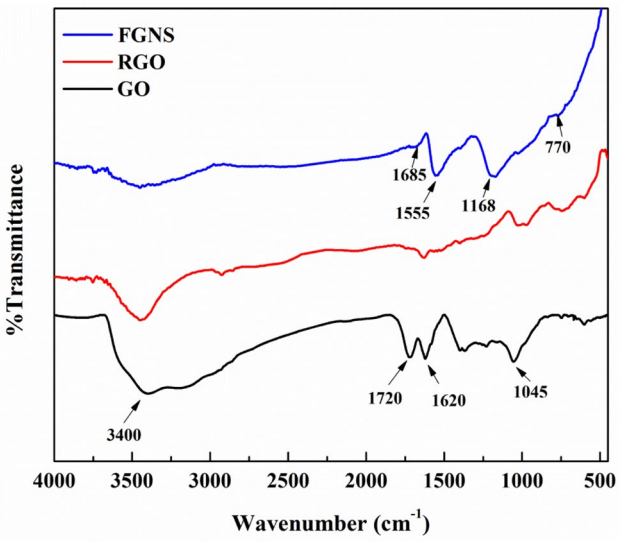

Fig. 2 FTIR spectra of GO, RGO, and FGNS

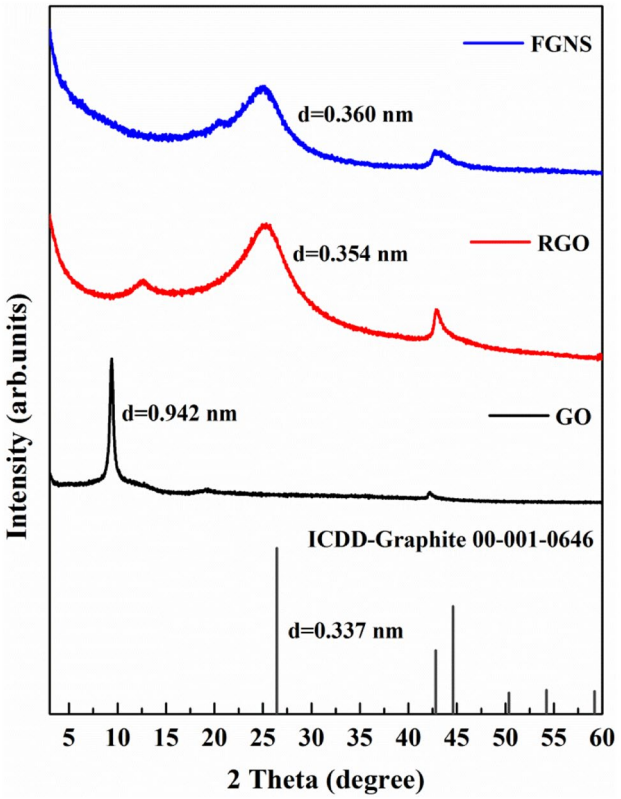

Fig. 3 XRD patterns of GO, RGO, and FGNS

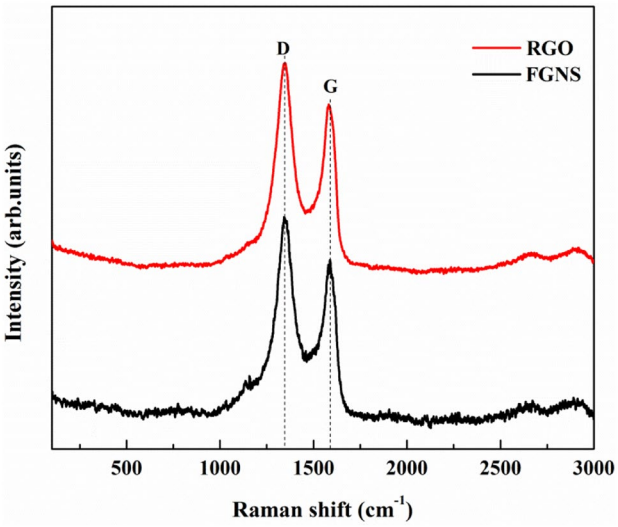

Fig. 4 Raman spectra of RGO, and FGNS

0.942 nm. This is significantly greater as against the interlayer space of graphite (0.337 nm) due to the intercalation of oxygen functional groups between the layers [47]. Thermal reduction of GO results in the diffraction peaks at 12.5°, 25.20°, and 42.9° that correspond to the (001), (002), and (100) crystal planes of RGO, respectively. The weak peak at 12.5° (001) arises due to the remnant oxygen functional groups that were not completely eliminated during the thermal reduction process [48]. Further, the XRD pattern of RGO exhibits broadening and shifting of diffraction peak (002) to 25.20° with reduced interlayer space value of 0.354 nm as against the 9.41° (001) and 0.942 nm of GO. This reduction in the interlayer space value of RGO could be due to elimination of the most of the oxygen functional groups between the layers that subsequently led to the restacking of graphene sheets. Compared to RGO, the FGNS exhibit a broadening and marginal shift in the diffraction peak (002) from 25.20° to 24.78°. Also, the functionalization of RGO led to the introduction of additional oxygen-containing functional groups (−COOH) on the graphene sheets that led to the increment of interlayer space value from 0.354 nm (RGO) to 0.360 nm in the FGNS.

Raman spectroscopy was used to assess the structural changes from RGO to FGNS, as shown in Fig. 4. Raman spectra of both RGO and FGNS exhibit characteristic D and G bands. The D band arises from the breathing modes of sp^2 rings and is initiated by the defects/disorders in the graphite lattice, and the G band corresponds to the first-order scattering of E_{2g} mode of sp^2 carbon atoms [49]. The Raman spectrum of RGO exhibits the D-band at 1346 cm^{-1} and a G-band at 1580 cm^{-1}, with an intensity ratio (I_D/I_G) of 1.22. After functionalizing RGO, the D- and G-bands were observed at 1346 cm^{-1} and 1587 cm^{-1}, respectively, with an intensity ratio (I_D/I_G) of 1.18. The intensity ratio of D and G bands (I_D/I_G) is used to measure the degree of disorder/defects. The intensity ratio (I_D/I_G) of FGNS was lower in comparison with that of RGO. This was possibly due to the contribution of a larger amount of sp^2 carbon atoms from the grafted aromatic structure of benzoate that outweighs the net amount of transformed sp^3 carbon atoms in the FGNS. This functionalization of RGO does not induce any additional defects in the graphene domains. The results demonstrated here agree well with earlier literature on functionalized RGO [50].

The surface morphological characteristics of RGO and FGNS were imaged under FESEM and are shown in Fig. 5a, b. The micrograph of RGO displayed layered stacks of nanosheets with irregular, lightly crumpled, and folded structures that can be attributed to the intrinsic thermal stability of 2-D structured graphene (Fig. 5a). However, the FGNS surface morphology (graphite-rose) showed the dominance of corrugated and wrinkled structure that is predominant on the edges of the sheet, resulting from the grafting of carboxylic groups via the functionalization route (Fig. 5b). This is further corroborated via TEM analysis of the FGNS that demonstrates the lamellar structure with the folding of

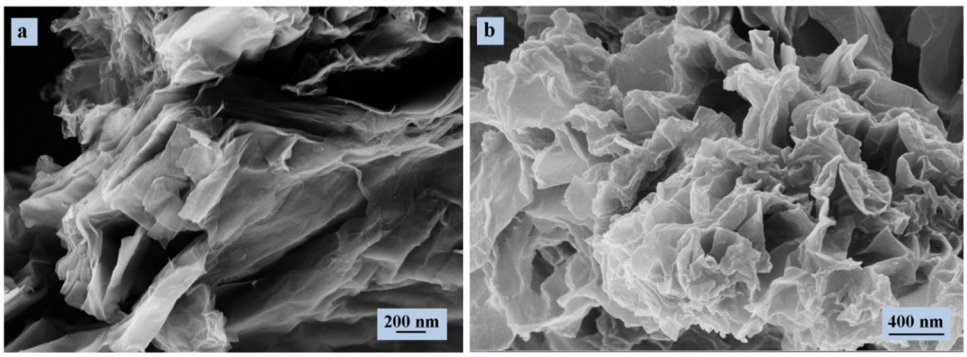

Fig. 5 FESEM images of **a**) RGO and **b**) FGNS

graphene sheets (Fig. 6a, b). The dark regions represent the crumpled structure that is formed by the stacking of several graphene nanosheets. The lateral dimensions of the nanosheets range from a few nanometers to several micrometers. The selected area diffraction pattern (SAED) of FGNS shows its polycrystalline nature (Fig. 6c). Additionally, the lattice fringes measure the interlayer space value of 0.360 nm (that belongs to the (002) plane), which is well in agreement with the XRD results of FGNS (Fig. 6d).

Characterization of TGP-based nanofabrics

FESEM results

The FESEM micrographs of TGP-based nanofabrics with varying FGNS content (0, 0.05, 0.10, 0.15, and 0.20 wt%) are shown in Fig. 7a–e. Electrospun PVDF (E-PVDF) and TGP-based nanofabrics demonstrated a bead-free morphology, with E-PVDF displaying a mean fiber diameter (MFD) of 397 ± 56 nm. On the contrary, the TGP-based

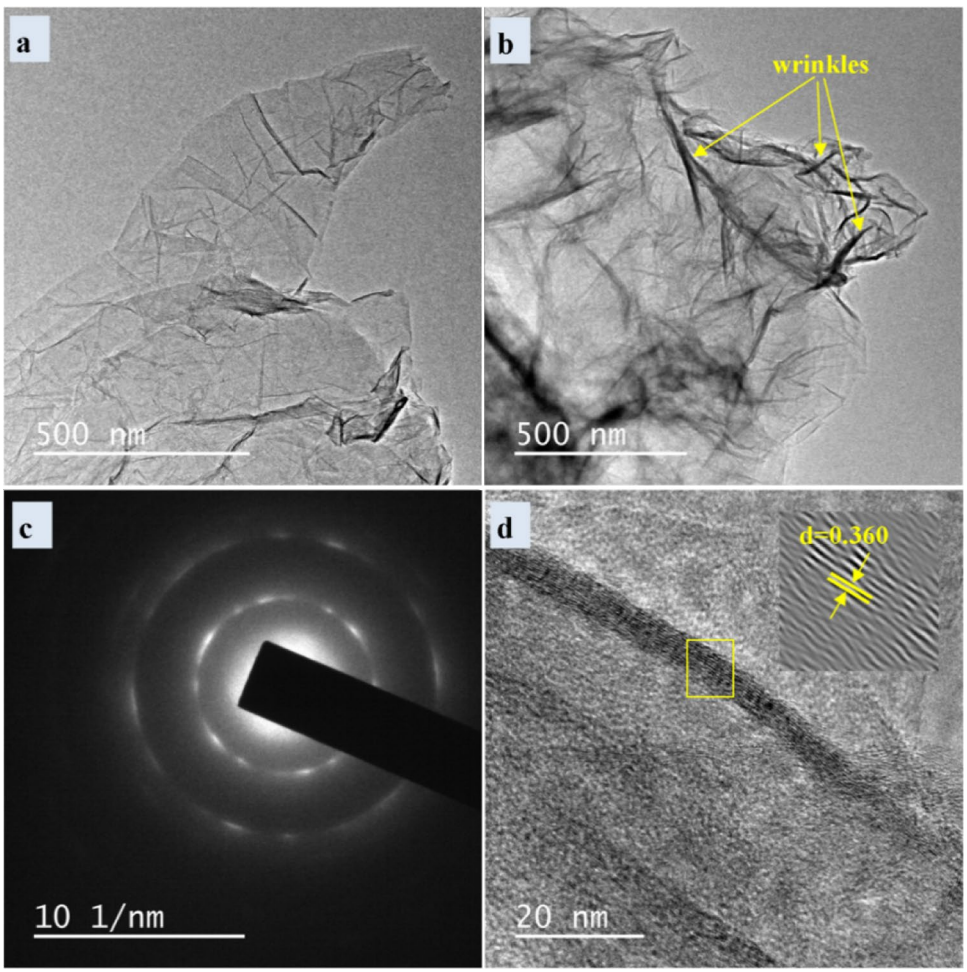

Fig. 6 Microstructure analysis of FGNS: (**a**, **b**) TEM images with yellow arrows indicating the wrinkled structure, (**c**) SAED pattern, and (**d**) d-space value from TEM image

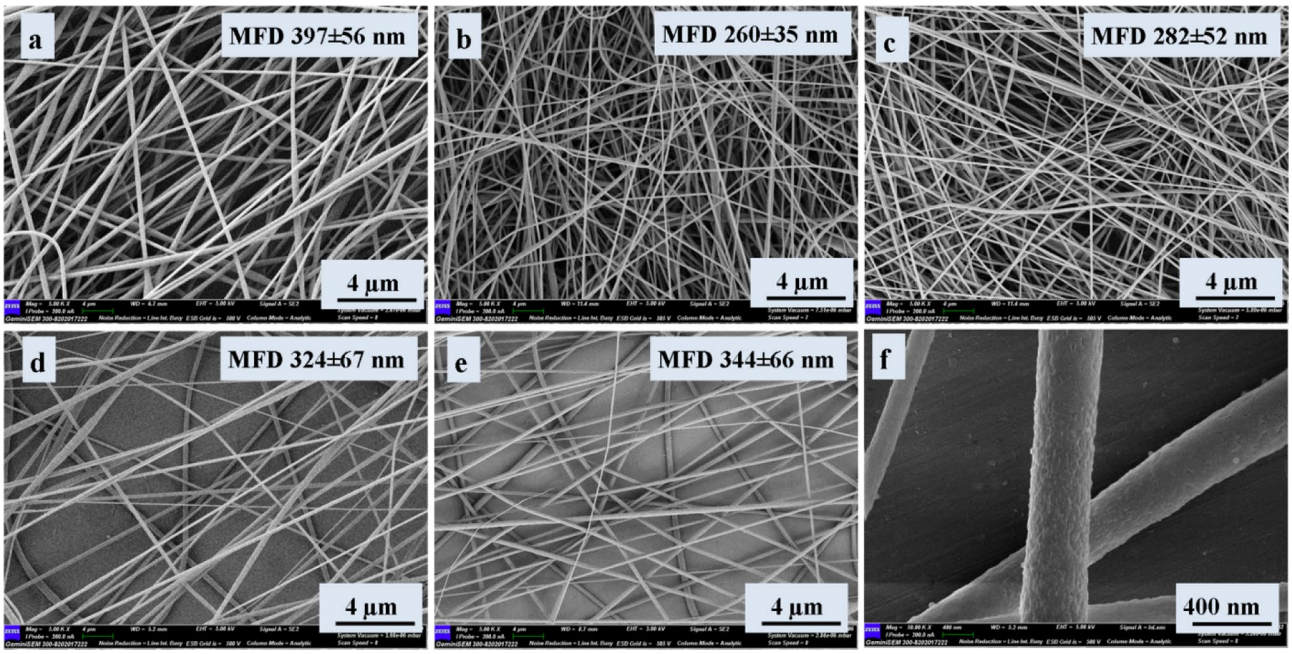

Fig. 7 FESEM micrographs of electrospun nanofabrics: **a**) E-PVDF; **b**) TGP-0.05; **c**) TGP-0.10; **d**) TGP-0.15; **e**) TGP-0.20; **f**) high magnification FESEM image of TGP-0.20

nanofabrics exhibited a reduction in MFD compared to the E-PVDF. This is attributed to the increased electrical conductivity and viscosity of the electrospinning solution in the presence of talc nanosheets and FGNS [29, 51]. Throughout electrospinning, the increased electrical conductivity of the solution causes longer stretching of the nanofibers resulting in reduced fiber diameters. While the viscosity of the solution increases, the viscoelastic forces resist the stretching of the nanofiber and lead to formation of thicker fibers. Hence, the balance between the viscoelastic and charge repulsion forces during electrospinning could significantly influence the morphology of nanofibers. As reported from the previous findings, graphene was demonstrated to improve the electrical conductivity and viscosity of the electrospinning solutions [32, 52]. In the current work, the increased content of FGNS loading in TGP-based nanofabrics had a significant effect on the viscosity of the solution that contributed to the increased fiber diameters. A high magnification SEM micrograph of TGP-0.20 based fiber displayed (Fig. 7f) a rough surface with a sheet-like texture, possibly due to the inclusion of talc nanosheets and graphene in the PVDF matrix. The electrostatic stretching effect induced during electrospinning ensures the alignment and embedding of the fillers within the PVDF matrix. Additionally, improving the interfaces of FGNS with the PVDF matrix facilitates the chemical interaction between them. This is further corroborated by the EDS elemental mapping of TGP-0.10 based nanofabrics that display improved dispersion of fillers without any possible aggregation in the PVDF matrix (Fig. 8).

XRD results

Figure 9 represents the XRD patterns of E-PVDF and TGP-based nanocomposite nanofabrics. E-PVDF displays the diffraction peak at $2\theta = 18.4°$ and 20.4°, which correspond to the (020) and (110/200) crystal planes of α- and β-phases of PVDF, respectively [53]. With the introduction of FGNS in TGP nanofabrics, the intensity of α peak weakens while the β peak intensifies. Notably, the characteristic α peak diminishes while β peak shifts to $2\theta = 20.6°$ for TGP-0.10 based nanofabrics, thereby indicating the probable interactions between the fillers and PVDF matrix. Additionally, the diffraction peaks at $2\theta = 9.4°$ and 28.6° displayed by the TGP nanofabrics correspond to the crystal planes (002) and (006) of talc nanosheets (ICDD-013–0558), thus confirming their presence in the former. XRD results imply the domination of the β-phase with the strong reflection peak at $2\theta = 20.6°$ and a weak peak at $2\theta = 36.3°$ for TGP-0.10 based nanofabrics compared to E-PVDF [54]. Thus the addition of FGNS facilitates the transformation of α- to β-phase of PVDF in the TGP-based nanofabrics.

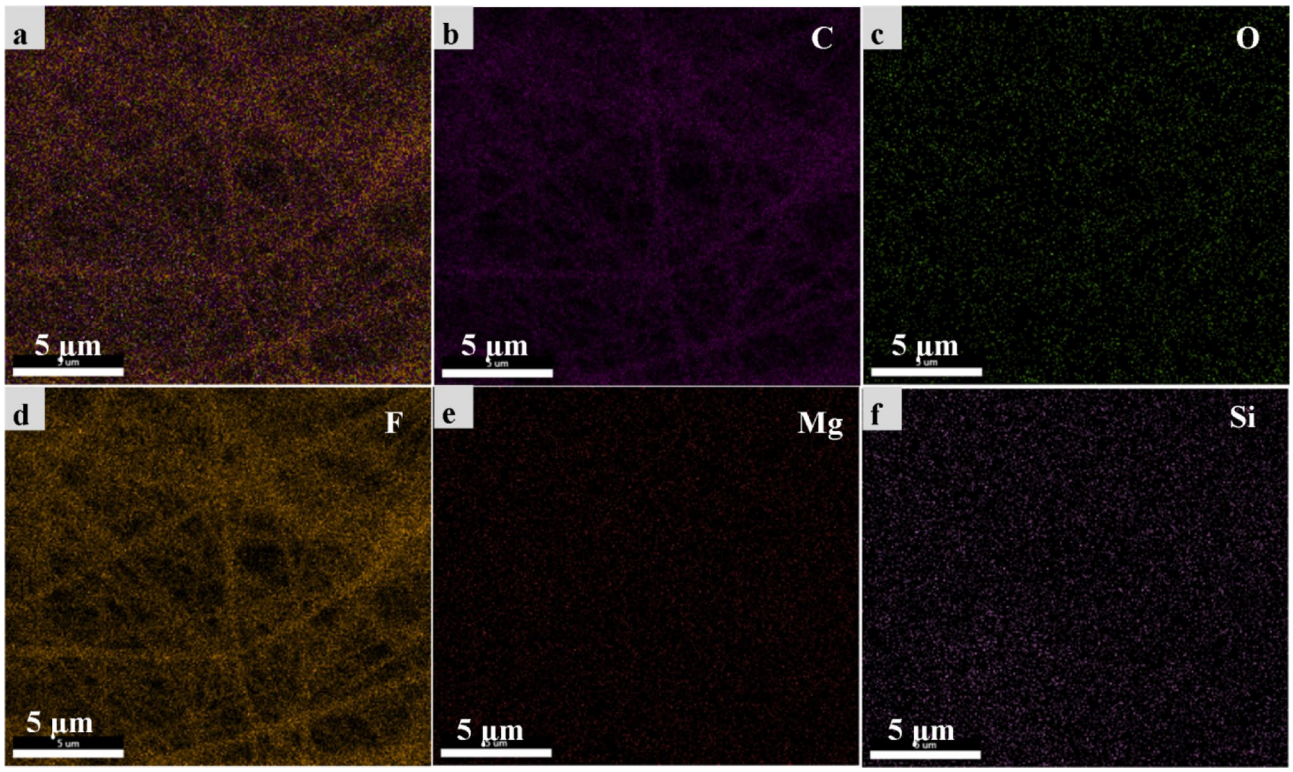

Fig. 8 EDS elemental mapping of TGP-0.10 nanofabrics: (**a**) overlay distributions of elements, (**b**) distribution of carbon, (**c**) distribution of oxygen, (**d**) distribution of fluorine, (**e**) distribution of magnesium, and (**f**) distribution of silicon

FTIR results

The enhancement of β-phase crystallization in the TGP nanofabrics is further confirmed via FTIR analysis. Evident from Fig. 10a, E-PVDF and TGP nanofabrics display absorption bands characteristic of the α-phase (763 and 975 cm^{-1}) and the β-phase (840, 1071, 1275, and 1401 cm^{-1}) of PVDF [29, 55]. The tiny peak at 1234 cm^{-1} corresponds to the γ-phase; however, other exclusive bands (776, 812, and 833 cm^{-1}) characteristic of the γ-phase are not evident in the present study [56]. Moreover, the presence of a prominent band at 1275 cm^{-1} that is characterstic of the β-phase exhibited by TGP nanofabrics substantiates the crystallization of the β-phase in the PVDF matrix. Considering the TGP nanofabrics majorly display the presence of the β-phase with traces of α-phase and negligible γ-phase, the relative β-phase fraction (F(β)) can be calculated using Eq. (1) [32].

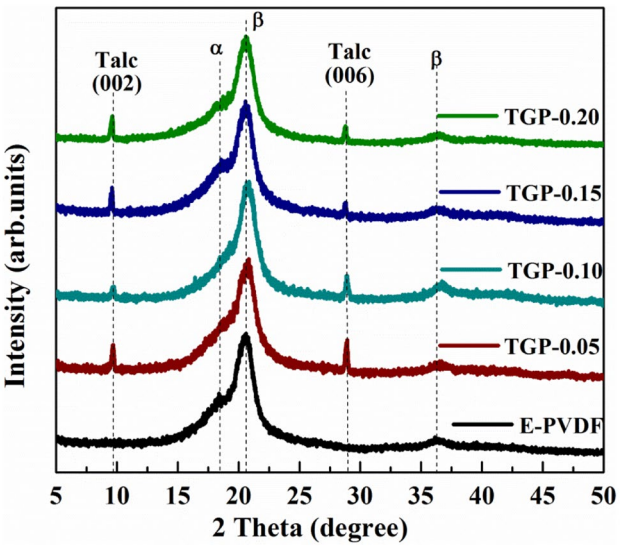

Fig. 9 XRD patterns of E-PVDF and TGP-based nanofabrics

$$F(\beta) = \frac{A_\beta}{\left(\frac{K_\beta}{K_\alpha}\right)A_\alpha + A_\beta} \times 100\% \quad (1)$$

where A_α and K_α (6.1×10^4 cm^2 mol^{-1}) are the absorption peak and coefficient values at 763 cm^{-1} (α-phase), at the same time, A_β and K_β (7.7×10^4 cm^2 mol^{-1}) are the absorption peak and coefficient values at 840 cm^{-1} (β-phase). The calculated F(β) values for E-PVDF and TGP nanofabrics are shown in Table 1. TGP nanofabrics demonstrated improved F(β) values compared to E-PVDF, with TGP-0.10 reaching a maximum of 90.2%. Thus the enhancement of F(β) values displayed by TGP

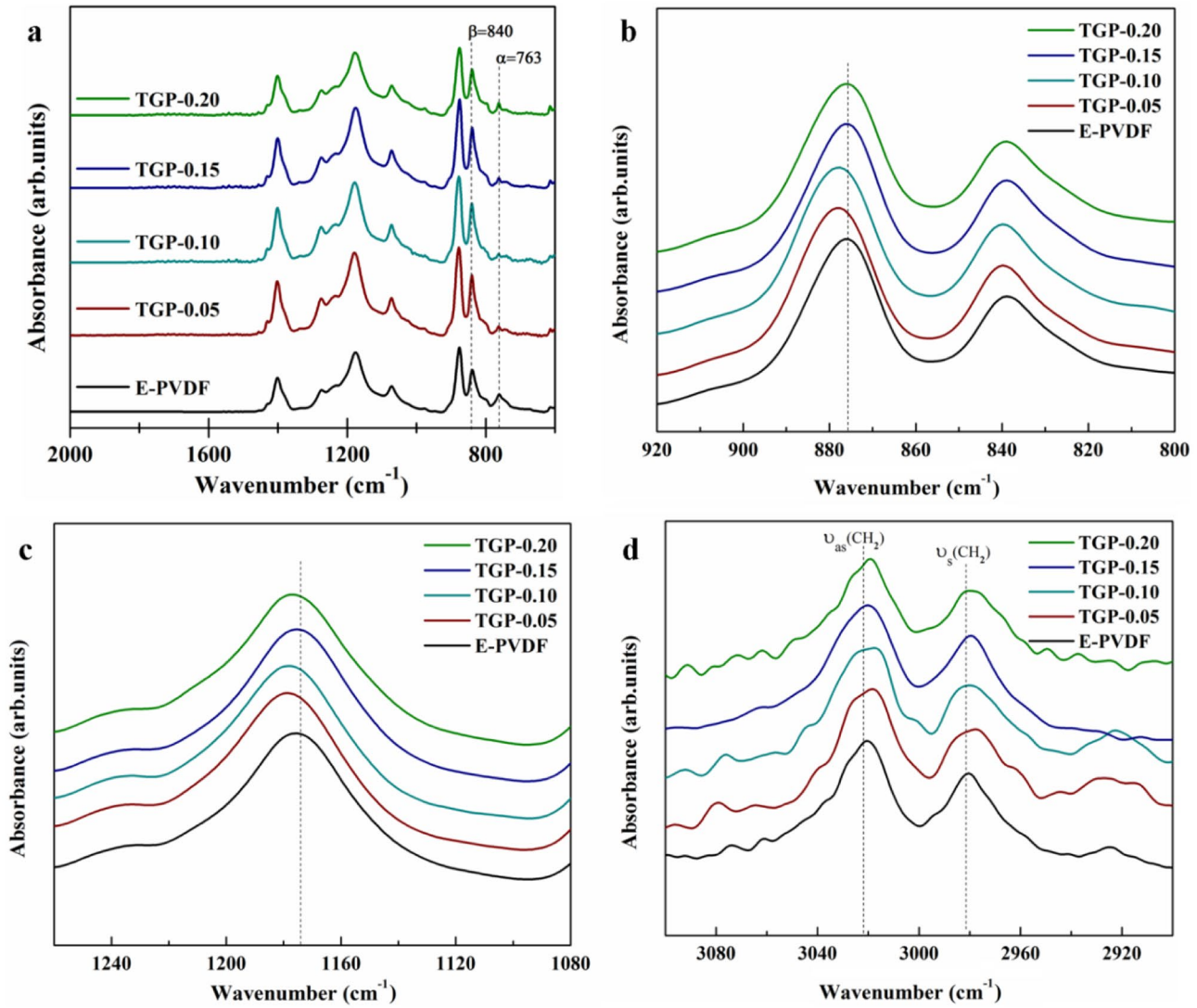

Fig. 10 FTIR spectra of E-PVDF and TGP-based nanofabrics in the wavenumber range of **a**) 2000–650 cm^{-1}, **b**) 920–800 cm^{-1}, **c**) 1250–1080 cm^{-1}, and **d**) 3100–2900 cm^{-1}

nanofabrics implies the facilitation of β-phase by the induced FGNS in the talc/PVDF matrix. This enhancement of β-phase in the TGP based nanofabrics can be ascribed to the strong interactions between the functional groups (− OH, − C = O, − COOH) on the graphene sheets/talc nanosheets and $–CF_2$ groups of PVDF. The vibrational bands at 875 and 1173 cm^{-1} associated with the CC asymmetric stretching and CF_2 symmetric stretching modes of E-PVDF shifted to 877–879 cm^{-1} and 1177–1179 cm^{-1}, respectively in the vibrational spectra of TGP- based

Table 1 β-phase fraction, crystallization temperature, melting temperature, degree of crystallinity, tensile strength, and Young's modulus of the E-PVDF and TGP-based nanofabrics

Sample	FTIR %β-phase	DSC			Mechanical property	
		T_c (°C)	T_m (°C)	X_c (%)	Tensile strength (MPa)	Young's modulus (MPa)
E-PVDF	61.4	141.5	171.7	55.4	12.70 ± 0.11	26.69 ± 0.23
TGP-0.05	87.7	142.6	174.8	48.4	13.70 ± 0.55	32.61 ± 0.74
TGP-0.10	**90.2**	**141.9**	**174.7**	**38.2**	**17.03 ± 2.58**	**53.41 ± 1.12**
TGP-0.15	82.6	141.7	174.8	51.0	17.49 ± 0.55	33.52 ± 2.21
TGP-0.20	76.9	142.6	174.3	42.8	19.43 ± 1.22	42.43 ± 0.44

nanofabrics (Fig. 10b, c) [57, 58]. Due to the higher electronegativity of fluorine as against carbon and hydrogen atoms of PVDF, the shifting of vibrational bands as mentioned ealier corroborates the strong interaction between the FGNS and PVDF chains; this interaction facilitates the transformation of trans-gauche-trans-gauche (TGTG) conformation of the α-phase to the all-trans conformation (TTTT), characteristic of the β-phase.

Further, the FTIR bands in the region of 3100–2900 cm^{-1} (Fig. 10d) were probed to ascertain the interfacial interactions between the FGNS and PVDF matrix. The $-CH_2$ stretching vibration bands [asymmetric (υ_{as}) and symmetric (υ_s)] of TGP-based nanofabrics shifted to lower wavenumbers when compared with that of the E-PVDF, affirming the interfacial interactions between the filler and the polymer matrix. The shifting of the bands mentioned above could be ascribed to the damping of the stretching vibrations of $-CH_2$ dipoles, and accordingly the damping coefficient (r_{dc}) is calculated using Eq. 2 [59].

$$r_{dc} = 4\pi c\sqrt{(\vartheta_{PVDF}^2 - \vartheta_{TGP}^2)} \tag{2}$$

where c is the velocity of light, ϑ_{PVDF} is the wavenumber of E-PVDF with damping-free stretching vibrations of $-CH_2$ dipoles, and ϑ_{TGP} is the wavenumber of TGP-based nanofabrics exhibiting damped stretching vibrations of $-CH_2$ dipoles. The damping coefficient (r_{dc}) increases and attains the maximum value for TGP-0.10 nanofabrics and decreases thereafter (Fig. S3, ESI). This is ascribed to the attainment of percolation threshold loading of FGNS at the loading of 0.10 wt% in the PVDF matrix. The increased damping coefficient (r_{dc}) displayed by TGP-0.10 nanofabrics indicates good interfacial interaction, which promotes the electroactive β-phase of PVDF. The probable mechanism of interaction between the hybrid fillers (TNS and FGNS) and the PVDF matrix is represented in Fig. 11.

DSC results

Figure 12a, b shows the DSC curves during the cooling and heating cycles for E-PVDF and TGP-based nanofabrics with their corresponding melting temperatures (T_m), crystallization temperature (T_c), and degree of crystallinity (X_c) as listed in Table 1. The value of X_c was calculated using Eq. 3.

$$X_c = \frac{\Delta H_m}{\Delta H_{100}} \times 100\% \tag{3}$$

Here, ΔH_m and ΔH_{100} are the melting enthalpies of the nanofabric samples and 100% crystalline PVDF (104.7 J/g), respectively [60]. Evidently, for TGP-based nanofabrics, the T_m and T_c values shifted to a higher temperature than E-PVDF. This can be attributed to the inclusion of well-dispersed filler particles that act as nucleation sites, which promote the crystallization of PVDF. However, the X_c values of TGP-based nanofabrics decreased as against the E-PVDF. This may be ascribed to a larger number of nuclei growth initiated by the nucleating agents, which continue to grow in the limited space of the nanofiber during electrospinning, subsequently leading to smaller spherulites. Thus, the growth of these nuclei results in more crystal defects that reduce the degree of

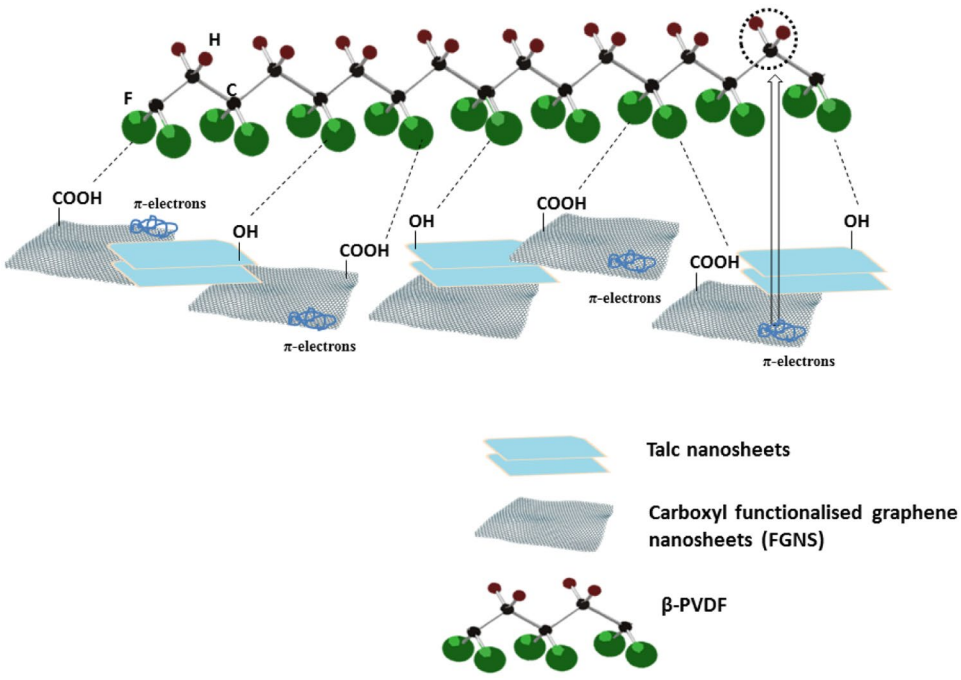

Fig. 11 Schematic illustration of plausible interactions between hybrid fillers and PVDF

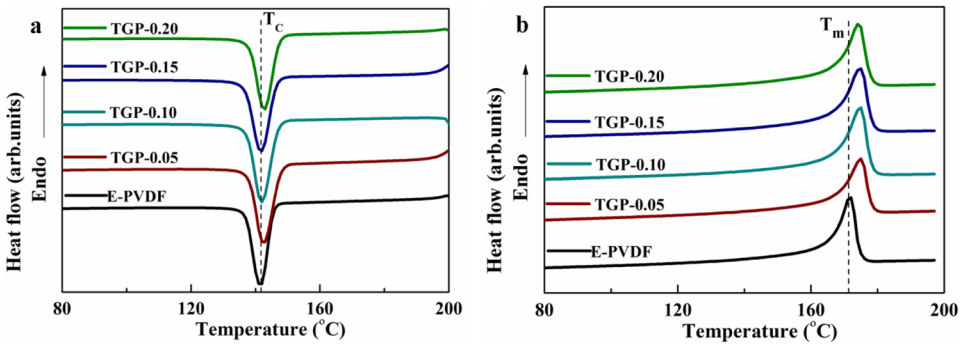

Fig. 12 DSC traces of E-PVDF and TGP-based nanofabrics: (**a**) Cooling cycle; and (**b**) Heating cycle

crystallinity. Furthermore, the length, distribution, and curvature of filler hinder the mobility of PVDF chains, which also affects the X_c values. A similar trend in the decline of X_c values for graphene/PVDF-based systems was reported in the literature [61, 62].

Since the melting temperature range for the α- and β-crystallites of PVDF is similar (167–175 °C), the DSC will not be able to distinguish between these two phases [63]. However, DSC can be used to identify γ-phase in the TGP-based nanofabrics, as the melting peak of the same appears in the temperature range of 179–190 °C [64, 65]. Accordingly, the results of XRD, FTIR, and DSC together suggest the predominance of the β-phase in TGP-based nanofabrics.

Tensile testing results

The characteristic tensile stress–strain behavior of the E-PVDF and TGP-based nanofabrics is shown in the Fig. 13, with its mechanical properties summarized in Table 1. The addition of FGNS in TGP-based nanofabrics enhanced the tensile strength and Young's modulus of the latter. Graphene and its derivatives have been proven to improve the tensile properties of PVDF-based composites as the former offers higher aspect ratio, flexibility and Young's modulus [66, 67]. A low loading of 0.10 wt% FGNS in TGP-based nanofabrics resulted in a significant increment in tensile strength (17.03 ± 2.58 MPa) and Young's modulus (53.41 ± 1.12 MPa) while the strain at break was reduced, compared to E-PVDF. Moreover, the FGNS loading beyond 0.10 wt% in TGP-based nanofabrics displayed no significant enhancement in the mechanical properties. This is attributable to the possible restacking of graphene flakes due to van der Waals forces that promote the piling of graphene flakes at higher loading; and this subsequently impairs the mechanical properties the composite [68]. The enhancement of mechanical properties demonstrated by the TGP-based nanofabrics is ascribed to the following: first, the good dispersion of nanofillers (talc nanosheets and FGNS) in the PVDF matrix improves the filler–polymer interfacial contact. Second, the effective interaction between the $-CF_2$ groups of PVDF and hydroxyl groups of nanofillers via hydrogen bonding facilitates the stress transfer from the polymer matrix to the nanofillers. And third, the high aspect ratio offered by nanofillers restricts the movement of PVDF chains. Overall, the inclusion of FGNS in TGP-based nanofabrics increased the mechanical properties due to the compatibility of the former with the PVDF matrix.

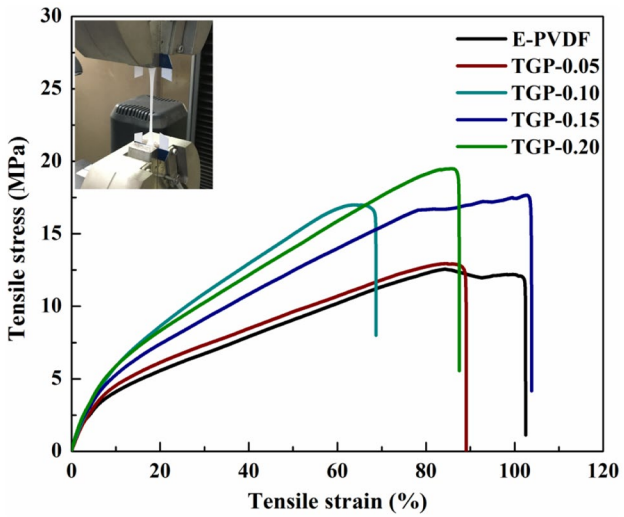

Fig. 13 Tensile stress–strain plots of E-PVDF and TGP-based nanofabrics

Piezoelectric measurements

The flexoelectric effect is the induction of electrical polarization due to strain gradient evident in dielectric materials. Further, this effect is more significant at the nanoscale and has been demonstrated to enhance the piezoelectric response of the nanogenerator [69]. Thus, the flexoelectric effect possibly contributes to the piezoelectric performance of the TGP-based nanogenerator. The nanogenerators based on the E-PVDF and TGP nanofabrics were imparted with compression force using a pneumatic actuator (operating pressure 0.4 MPa) setup (Fig. S2, ESI) and their corresponding piezoelectric responses are shown in Fig. 14a. TGP based

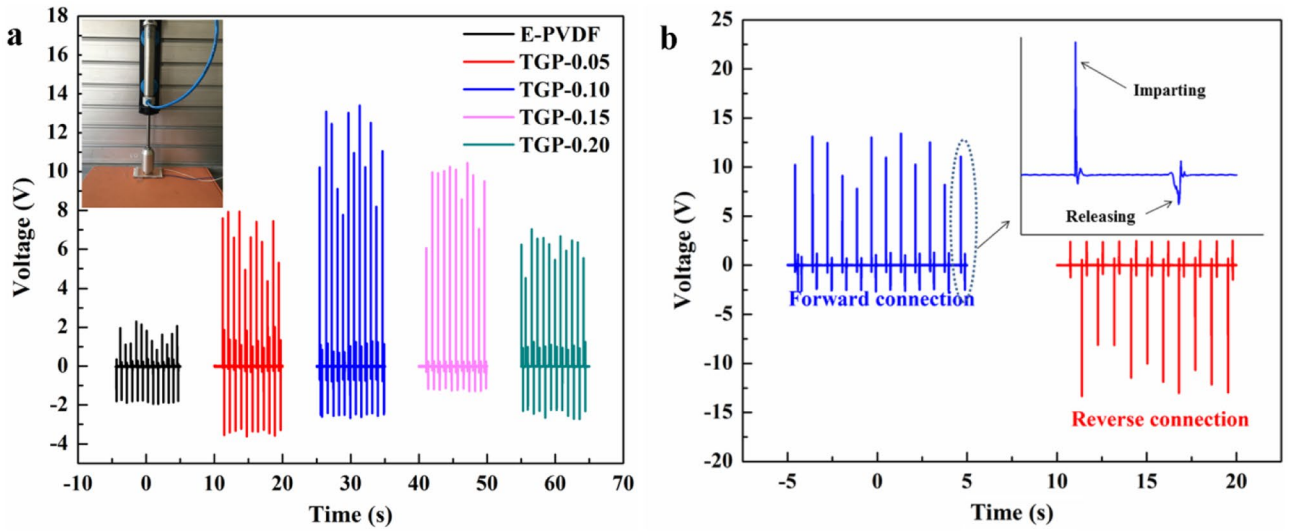

Fig. 14 **a**) The output voltage generated from E-PVDF and TGP-based nanofabrics under impact by pneumatic actuator mode, **b**) switching polarity sequence test of TGP-0.10 nanofabrics with inset displaying magnified impacting and releasing responses

nanofabrics demonstrated a significant enhancement in the piezoelectric potential when compared to virgin PVDF nanofabrics, with TGP-0.10 reaching a maximum open-circuit voltage of 12.9 V. In contrast, E-PVDF displayed the open-circuit voltage of 2.0 V. The piezoelectric performance of the nanogenerator is enhanced with an increase in FGNS loading up to 0.10 wt% beyond which the piezoelectric output voltage decreased. The declined piezoelectric performance of the TGP nanofabrics at higher FGNS loading may be attributed to the filler aggregation leading to leakage of charges through the conducting FGNS networks in the PVDF matrix.

Figure 14b shows the switching polarity sequence with voltage amplitudes implying the mechanical imparting and releasing modes on the nanogenerator comprised of TGP-0.10 nanofabrics. Evidently, the imparting mode voltage amplitude is greater compared to release amplitude, as the former is proportional to the impact force while the latter is dependent on the elasticity of the material. The switching polarity sequence demonstrated by the TGP based nanogenerator confirms that the output signals stemmed solely from the piezoelectric response of TGP nanofabrics. When the nanogenerator composed of electrospun nanofabrics is excited via a compressive strain in vertical direction, positive and negative piezoelectric potentials are produced on the top and bottom electrodes of the nanogenerator, respectively. The potential difference between the nanogenerator electrodes causes the charges to flow between the electrodes through an external circuit resulting in an electrical signal. The moment the compressive strain is released the piezoelectric potential difference between the electrodes vanishes and the accumulated charges flow in opposite direction resulting in a reverse electrical signal. Figure 15a displays the working mechanism of the nanogenerator under the mechanical impact and releasing modes.

Further, the power density of the TGP-0.10 based nanogenerator was measured by connecting the nanogenerator across different load resistances (0.1–5 MΩ) and noticing the voltage drop across the same as illustrated in Fig. 15b. Under the mechanical imparting mode, TGP-0.10 based nanogenerator produced a maximum voltage of 8.8 V across a load resistance of 3 MΩ. Accordingly, the instantaneous power density (P) was measured to be 1.72 μW/cm^2 and calculated using the Eq. 4.

$$P = \frac{V^2}{R_L A} \tag{4}$$

where V is the voltage drop across the load resistance R_L and A is the effective area (15 cm^2). Figure 16b shows the output voltage and power density generated from TGP-0.10 based nanogenerator across varying load resistance. The piezoelectric performance of TGP based nanogenerator is higher or comparable with that of the ones hitherto reported in the literature (Table 2). This increment in the open-circuit voltage and power density displayed by TGP-0.10 nanofabrics can be ascribed to the higher β-phase fraction and easier alignment of the $-CH_2/-CF_2$ dipoles due to the uniformly dispersed networks of talc nanosheets and FGNS in the PVDF matrix. Further, the electrical conductivity of the E-PVDF and TGP-based nanofabrics was measured (Sect. S4, ESI). The electrical conductivity of the TGP nanofabrics reached a maximum value at FGNS loading of 0.10 wt %, beyond which there was a marginal decrease in it (Fig S4, ESI). The inherent electrical conductivity of FGNS

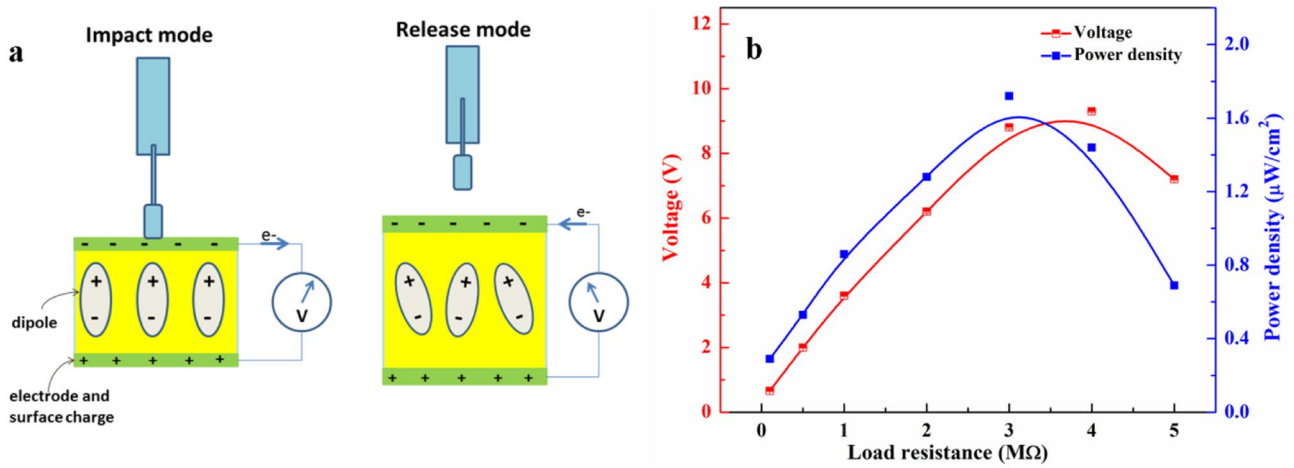

Fig. 15 **a**) working mechanism of the nanogenerator under impact and release mode; **b**) generated output voltage and power density as a function of varying load resistance from a TGP-0.10 based nanogenerator

led to the higher conductivity at a lower percolation threshold that boosted the piezoelectric performance of TGP-0.10 based nanofabrics. Further, the rough and porous surface morphology of TGP-0.10 based nanofibers possibly contributed to their improved piezoelectric response (Sect. S5, ESI).

PFM results

PFM was used to probe the local piezoelectric response of the TGP-based nanofabrics at the nanoscale. In PFM, a single nanofiber was subjected to a bias voltage, and its corresponding electromechanical response was recorded in terms of PFM

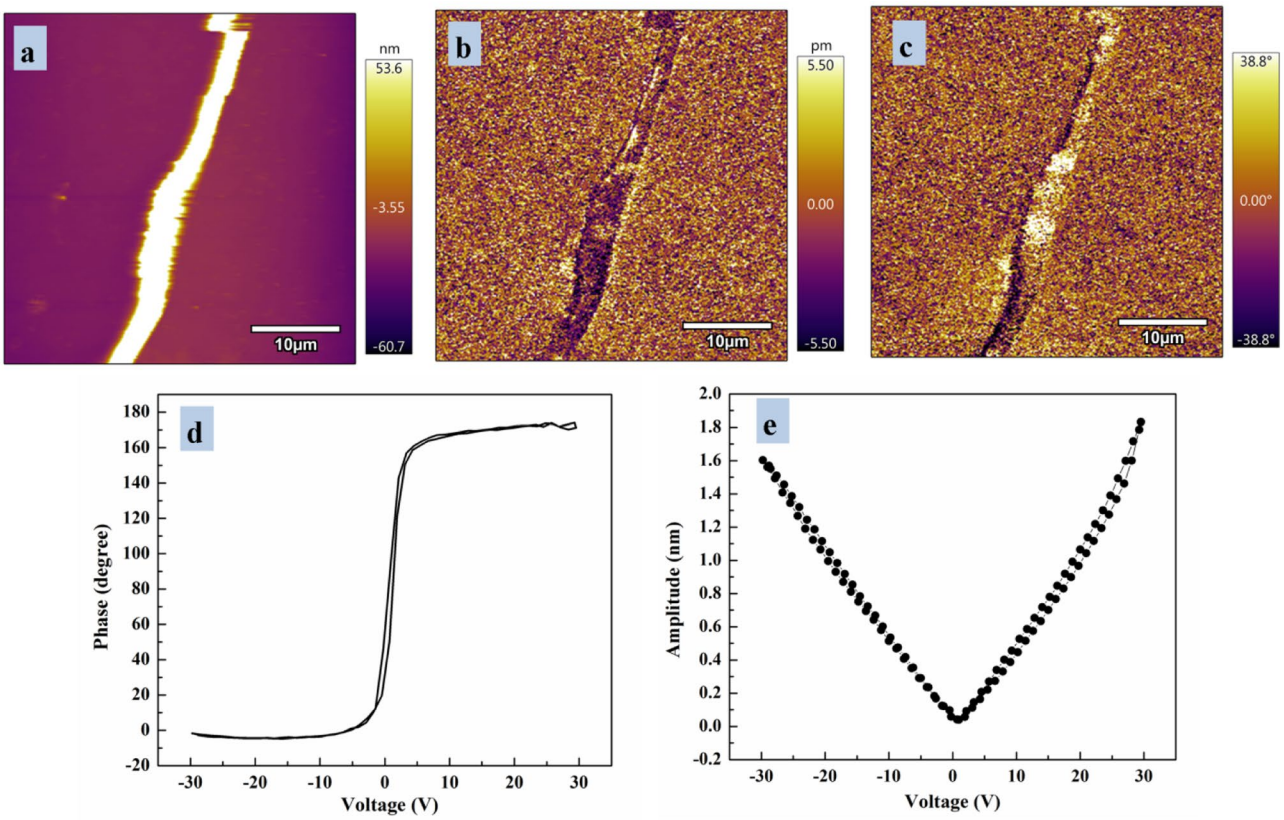

Fig. 16 PFM analysis of TGP-0.10: (**a**) topography image, (**b**) amplitude image, (**c**) phase image, (**d**) amplitude loop, and (**e**) phase loop

Table 2 Comparison of the piezoelectric performance of the TGP-based nanofabrics with that of the other PVDF-based systems

Type of materials	Output Voltage	Power density	Piezoelectric coefficient (d_{33})	Reference
(2 wt%) Fe-RGO/PVDF nanocomposite film	5.1 V	-	-	[72]
(0.1 wt%) Graphene/PVDF composite nanofibers	7.9 V	-	-	[27]
(1 wt%) Ag-CNT/PVDF composite nanofibers	-	-	54 pm/V	[73]
(1 wt%) RGO-Ag/PVDF nanocomposite films	18 V	28 μW/cm^3	-	[30]
(1 wt%) RGO/$NaNbO_3$/PVDF nanocomposite films	2.16 V	-	-	[74]
(0.5 wt%) TiO_2/PVDF composite nanofibers	11.5 V	-	39 pm/V	[18]
(1 wt%) GOCOOH/PVDF composite nanofibers	-	-	46 pm/V	[70]
(30 wt%) Modified potassium sodium Niobate/PVDF nanocomposite films	18 V	-	53 pm/V	[75]
(0.50 wt%) Talc nanosheets/PVDF nanocomposite fabrics	9.1 V	1.12 μW/cm^2	-	[29]
(3 wt%) Ni-Co LDH/PVDF nanocomposite fibers	6.9 V	0.92 μW/cm^2	-	[76]
(0.40 wt%) $CaCO_3$/(0.03 wt%) montmorillonite/PVDF nanocomposite	-	-	7.4 pm/V	[31]
(17.5 wt%) PANi/(10 wt%) HNT / PVDF nanocomposite fibers	7.2 V	0.25 μW/cm^2	-	[20]
(0.50 wt%) Talc/(0.10 wt%) FGNS / PVDF nanocomposite nanofabrics	**12.9 V**	**1.72 μW/cm^2**	**61 pm/V**	**This work**

amplitude and phase data. The PFM amplitude and phase data yield the material's local strain and polarization responses, respectively. PFM evaluated the nanoscale electromechanical behavior of the TGP-0.10 based single nanofiber with topography, amplitude, and phase responses as a function of bias voltage -30 V to + 30 V, as represented in the Fig. 16a–c. The phase image (Fig. 16c) displays regions of different contrast (bright and dark) indicating the polarization directions; the corresponding phase hysteresis loop (Fig. 16d) represents 180° domain switching behavior, indicating the ferroelectric response of TGP nanofiber. The phase switches by 180° at the coercive voltage (~ 0.9 V), beyond which the phase loop saturates. Furthermore, the amplitude signal (Fig. 16e) from TGP nanofiber depicts the butterfly-shaped characteristics loop resembling its piezoelectric property. The variation of amplitude response equals the strain changes (S) under the external electrical field (E); thus, the piezoelectric coefficient (d_{33}) of the TGP nanofiber can be calculated using the formula $S = d_{33}E$ [70]. From Fig. 16e, the maximum amplitude for TGP-0.10 nanofiber is 1.83 nm at 30 V, and accordingly, the calculated d_{33} is 61 pm/V, which is much higher than that of E-PVDF with d_{33} value of 10 pm/V. Similarly, the piezoelectric coefficient values for TGP-0.05, TGP-0.15, and TGP-0.20 based nanofibers were measured to be 45 pm/V, 38 pm/V, and 36 pm/V, respectively (Fig. S6, ESI).

According to Eq. 5, the output voltage (V) is dependent on the material's piezoelectric coefficient, Young's modulus (E), applied strain (ε), and charge separation distance/nanofiber diameter (d) [71]. Thus, the significant output voltage exhibited by TGP-based nanofabrics can be accounted to its reduced fiber diameter and higher Young's modulus when compared against E-PVDF nanofabrics.

$$V = \frac{d_{33}E_{33}\varepsilon_3 d}{k} \tag{5}$$

Further, the interactions between the oxygen containing functional groups (−OH, −COOH) of the hybrid fillers (talc nanosheets and FGNS) and $-CF_2/-CH_2$ groups of PVDF matrix enable the orientation of the all-trans β-phase. Also, the conducting path provided by FGNS in the host matrix would reduce the internal resistance of the nanogenerator and thereby facilitate the movement of induced charges generated by the PVDF. Herein, talc nanosheets facilitated the β-phase conformation and aided in the dispersion of FGNS in the PVDF matrix. In contrast, the FGNS provided conductive network for easy movement of induced charges in the polymer matrix and partly contributed to the β-phase fraction enhancement via interaction with PVDF. Thus these hybrid fillers synergistically improved the performance of PVDF-based composite nanofabrics.

Conclusions

In summary, a flexible hybrid filler/PVDF based nanocomposite fabric was successfully fabricated by electrospinning. Synergistic effects of talc nanosheets and carboxyl functionalized graphene nanosheets contributed to the enhanced piezoelectric response of the PVDF-based nanocomposite nanofabrics. A low loading of 0.10 wt% of FGNS in TGP-based nanofabrics led to a significant improvement in the β-phase fraction, mechanical property, and piezoelectric performance when compared against E-PVDF nanofabrics. Further, the nanogenerator based on electrospun nanofabrics

with 0.5 wt% of TNS and 0.10 wt% of FGNS demonstrated a peak output voltage of 12.9 V and a maximum power density of 1.72 μW/cm^2 under instrumented mechanical impact. TGP-0.10 based nanofibers exhibited the piezoelectric coefficient (d_{33}) value of 61 pm/V, that being 6 times higher than the E-PVDF nanofibers (10 pm/V). The uniform distribution and effective interactions of hybrid fillers (talc nanosheets and FGNS) with the PVDF matrix led to the promotion of all-trans conformation of β-phase. The developed hybrid nanocomposite nanofabrics could be a promising material in designing portable and flexible electronic devices.

Supplementary information The online version contains supplementary material available at https://doi.org/10.1007/s10965-021-02786-6.

Acknowledgements Sawan Shetty acknowledges and thanks NITK, Surathkal for a research scholarship. The authors acknowledge Prof. Udaya Bhat K for providing FESEM and TEM facilities. The authors acknowledge Dr. M. R. Rahman for providing the XRD facility. The authors thankfully acknowledge Prof.K.N. Prabhu for providing the UTM facility. The authors thank and acknowledge BIO-AFM (BSBE)—IRCC BIO Atomic Force Microscopy (BIO-AFM) Central Facility of I.I.T. Bombay for providing with PFM facility. Sawan Shetty is thankful to Mr.Vijay Mistari for his technical assistance in PFM analysis. The authors are thankful to Ms.Prateeksha, Mr. Prajwal, and Mr. Augustine S for their assistance in SEM, TEM, and UTM analysis, respectively.

References

1. Wan C, Bowen CR (2017) Multiscale-structuring of polyvinylidene fluoride for energy harvesting: the impact of molecular-, micro- and macro-structure. J Mater Chem A 5:3091–3128
2. Hu D, Yao M, Fan Y et al (2019) Strategies to achieve high performance piezoelectric nanogenerators. Nano Energy 55:288–304
3. Liu H, Zhong J, Lee C et al (2018) A comprehensive review on piezoelectric energy harvesting technology: Materials, mechanisms, and applications. Appl Phys Rev 5:041306
4. Chen X, Han X, Shen QD (2017) PVDF-based ferroelectric polymers in modern flexible electronics. Adv Electron Mater 3:1600460
5. Lovinger AJ (1983) Ferroelectric polymers. Science 220:1115–1121
6. Ruan L, Yao X, Chang Y et al (2018) Properties and applications of the β phase poly(vinylidene fluoride). Polymers (Basel) 10:1–27
7. Sencadas V, Gregorio R, Lanceros-Méndez S (2009) α to β phase transformation and microestructural changes of pvdf films induced by uniaxial stretch. J Macromol Sci Part B 48:514–525
8. Yu YJ, McGaughey AJH (2016) Energy barriers for dipole moment flipping in PVDF-related ferroelectric polymers. J Chem Phys 144:14901
9. Li L, Zhang M, Rong M, Ruan W (2014) Studies on the transformation process of PVDF from α to β phase by stretching. RSC Adv 4:3938–3943
10. Li Q, Ke W, Chang T, Hu Z (2019) A molecular ferroelectrics induced electroactive β-phase in solution processed PVDF films for flexible piezoelectric sensors. J Mater Chem C 7:1532–1543
11. Andrew JS, Clarke DR (2008) Effect of electrospinning on the ferroelectric phase content of polyvinylidene difluoride fibers. Langmuir 24:670–672
12. Zhao Z, Li J, Yuan X et al (2005) Preparation and properties of electrospun poly(vinylidene fluoride) membranes. J Appl Polym Sci 97:466–474
13. Jiyong H, Yinda Z, Hele Z et al (2017) Mixed effect of main electrospinning parameters on the β -phase crystallinity of electrospun PVDF nanofibers. Smart Mater Struct 26:85019
14. Ghafari E, Lu N (2019) Self-polarized electrospun polyvinylidene fluoride (PVDF) nanofiber for sensing applications. Compos Part B Eng 160:1–9
15. Wu CM, Chou MH (2016) Polymorphism, piezoelectricity and sound absorption of electrospun PVDF membranes with and without carbon nanotubes. Compos Sci Technol 127:127–133
16. Lee C, Wood D, Edmondson D et al (2016) Electrospun uniaxially-aligned composite nanofibers as highly-efficient piezoelectric material. Ceram Int 42:2734–2740
17. Li J, Chen S, Liu W et al (2019) High performance piezoelectric nanogenerators based on electrospun ZnO nanorods/poly(vinylidene fluoride) composite membranes. J Phys Chem C 123:11378–11387
18. Alam MM, Sultana A, Mandal D (2018) Biomechanical and acoustic energy harvesting from TiO_2 nanoparticle modulated PVDF nanofiber made high performance nanogenerator. ACS Appl Energy Mater 1:3103–3112
19. Shamitha C, Mahendran A, Anandhan S (2020) Effect of polarization switching on piezoelectric and dielectric performance of electrospun nanofabrics of poly(vinylidene fluoride)/Ca–Al LDH nanocomposite. J Appl Polym Sci 137:1–12
20. Khalifa M, Mahendran A, Anandhan S (2019) Durable, efficient, and flexible piezoelectric nanogenerator from electrospun PANi/HNT/PVDF blend nanocomposite. Polym Compos 40:1663–1675
21. Neppalli R, Wanjale S, Birajdar M, Causin V (2013) The effect of clay and of electrospinning on the polymorphism, structure and morphology of poly(vinylidene fluoride). Eur Polym J 49:90–99
22. Liu Y-L, Li Y, Xu J-T, Fan Z-Q (2010) Cooperative effect of electrospinning and nanoclay on formation of polar crystalline phases in poly(vinylidene fluoride). ACS Appl Mater Interfaces 2:1759–1768
23. Wu CM, Chou MH, Zeng WY (2018) Piezoelectric response of aligned electrospun polyvinylidene fluoride/carbon nanotube nanofibrous membranes. Nanomaterials 8:1–13
24. Yu H, Huang T, Lu M et al (2013) Enhanced power output of an electrospun PVDF/MWCNTs-based nanogenerator by tuning its conductivity. Nanotechnology 24:405401
25. Xu Z (2017) In: Zhu H (ed) Graphene: Fabrication, Characterizations, Properties and Applications, 1st edn. Elsevier, United Kingdom
26. Lee C, Wei X, Kysar JW, Hone J (2008) Measurement of the elastic properties and intrinsic strength of monolayer graphene. Science 321:385–388
27. Abolhasani MM, Shirvanimoghaddam K, Naebe M (2017) PVDF/graphene composite nanofibers with enhanced piezoelectric performance for development of robust nanogenerators. Compos Sci Technol 138:49–56
28. Zeyrek Ongun M, Oguzlar S, Doluel EC et al (2020) Enhancement of piezoelectric energy-harvesting capacity of electrospun β-PVDF nanogenerators by adding GO and rGO. J Mater Sci Mater Electron 31:1960–1968
29. Shetty S, Mahendran A, Anandhan S (2020) Development of a new flexible nanogenerator from electrospun nanofabric based on PVDF/talc nanosheet composites. Soft Matter 16:5679–5688
30. Pusty M, Sinha L, Shirage PM (2019) A flexible self-poled piezoelectric nanogenerator based on a rGO-Ag/PVDF nanocomposite. New J Chem 43:284–294

31. Jahan N, Mighri F, Rodrigue D, Ajji A (2018) Synergistic improvement of piezoelectric properties of PVDF/ $CaCO_3$/ montmorillonite hybrid nanocomposites. Appl Clay Sci 152:93–100
32. Shi K, Sun B, Huang X, Jiang P (2018) Synergistic effect of graphene nanosheet and $BaTiO_3$ nanoparticles on performance enhancement of electrospun PVDF nanofiber mat for flexible piezoelectric nanogenerators. Nano Energy 52:153–162
33. Peng Q-Y, Cong P-H, Liu X-J et al (2009) The preparation of PVDF/clay nanocomposites and the investigation of their tribological properties. Wear 266:713–720
34. Liu L, Wang Y, Alhassan S et al (2018) Clay-facilitated aqueous dispersion of graphite and poly(vinyl alcohol) aerogels filled with binary nanofillers. Gels 4:8
35. Hummers WS, Offeman RE (1958) Preparation of graphitic oxide. J Am Chem Soc 80:1339
36. Ryu SH, Sin JH, Shanmugharaj AM (2014) Study on the effect of hexamethylene diamine functionalized graphene oxide on the curing kinetics of epoxy nanocomposites. Eur Polym J 52:88–97
37. López Guerra E, Shanmugharaj AM, Choi WS, Ryu SH (2013) Thermally reduced graphene oxide-supported nickel catalyst for hydrogen production by propane steam reforming. Appl Catal A Gen 468:467–474
38. Athanasekou C, Sapalidis A, Katris I et al (2019) Mixed Matrix PVDF/graphene and composite-skin pvdf/graphene oxide membranes applied in membrane distillation. Polym Eng Sci 59:262–278
39. Mirza-Aghayan M, Molaee Tavana M, Boukherroub R (2016) Sulfonated reduced graphene oxide as a highly efficient catalyst for direct amidation of carboxylic acids with amines using ultrasonic irradiation. Ultrason Sonochem 29:371–379
40. Park S, An J, Jung I et al (2009) Colloidal suspensions of highly reduced graphene oxide in a wide variety of organic solvents. Nano Lett 9:1593–1597
41. Nethravathi C, Rajamathi M (2008) Chemically modified graphene sheets produced by the solvothermal reduction of colloidal dispersions of graphite oxide. Carbon N Y 46:1994–1998
42. Khalili D (2016) Graphene oxide: A promising carbocatalyst for the regioselective thiocyanation of aromatic amines, phenols, anisols and enolizable ketones by hydrogen peroxide/KSCN in water. New J Chem 40:2547–2553
43. Samsonowicz M, Hrynaszkiewicz T, Świsłocka R et al (2005) Experimental and theoretical IR, Raman, NMR spectra of 2-, 3- and 4-aminobenzoic acids. J Mol Struct 744:345–352
44. Coates J (2006) Interpretation of Infrared Spectra, A Practical Approach. Encycl Anal Chem 10815–10837
45. Guo R, Qi L, Mo Z et al (2017) A new route to synthesize polyaniline-grafted carboxyl-functionalized graphene composite materials with excellent electrochemical performance. Iran Polym J 26:423–430
46. Griffete N, Dechézelles JF, Scheffold F (2012) Dense covalent attachment of magnetic iron oxide nanoparticles onto silica particles using a diazonium salt chemistry approach. Chem Commun 48:11364–11366
47. Jiao X, Qiu Y, Zhang L, Zhang X (2017) Comparison of the characteristic properties of reduced graphene oxides synthesized from natural graphites with different graphitization degrees. RSC Adv 7:52337–52344
48. Fu C, Zhao G, Zhang H, Li S (2013) Evaluation and characterization of reduced graphene oxide nanosheets as anode materials for lithium-ion batteries. Int J Electrochem Sci 8:6269–6280
49. Behzadi M, Mahmoodi Hashemi M, Roknizadeh M et al (2021) Copper(ii) ions supported on functionalized graphene oxide: an organometallic nanocatalyst for oxidative amination of azolesviaC-H/C-N bond activation. New J Chem 45:3242–3251
50. Zhang B, Chen Y, Liu G et al (2012) Push-Pull archetype of reduced graphene oxide functionalized with polyfluorene for nonvolatile rewritable memory. J Polym Sci Part A Polym Chem 50:378–387
51. Lee H, Nagaishi T, Phan DN et al (2017) Effect of graphene incorporation in carbon nanofiber decorated with TiO_2 for photoanode applications. RSC Adv 7:6574–6582
52. Shan C, Wang Y, Xie S et al (2019) Free-standing nitrogen-doped graphene-carbon nanofiber composite mats: electrospinning synthesis and application as anode material for lithium-ion batteries. J Chem Technol Biotechnol 94:3793–3799
53. Chi Q, Zhou Y, Yin C et al (2019) A blended binary composite of poly(vinylidene fluoride) and poly(methyl methacrylate) exhibiting excellent energy storage performances. J Mater Chem C 7:14148–14158
54. Cai X, Lei T, Sun D, Lin L (2017) A critical analysis of the α, β and γ phases in poly(vinylidene fluoride) using FTIR. RSC Adv 7:15382–15389
55. Mandal A, Nandi AK (2013) Ionic liquid integrated multiwalled carbon nanotube in a poly(vinylidene fluoride) matrix: Formation of a piezoelectric β-polymorph with significant reinforcement and conductivity improvement. ACS Appl Mater Interfaces 5:747–760
56. Gregorio R (2006) Determination of the α, β, and γ crystalline phases of poly(vinylidene fluoride) films prepared at different conditions. J Appl Polym Sci 100:3272–3279
57. Ulaganathan M, Rajendran S (2010) Preparation and characterizations of PVAc/P(VdF-HFP)-based polymer blend electrolytes. Ionics (Kiel) 16:515–521
58. Sharma M, Madras G, Bose S (2015) Contrasting effects of graphene oxide and poly(ethylenimine) on the polymorphism in poly(vinylidene fluoride). Cryst Growth Des 15:3345–3355
59. Abdalla S, Obaid A, Al-Marzouki FM (2016) Preparation and characterization of poly(vinylidene fluoride): A high dielectric performance nano-composite for electrical storage. Results Phys 6:617–626
60. Liu J, Lu X, Wu C (2013) Effect of preparation methods on crystallization behavior and tensile strength of poly(vinylidene fluoride) membranes. Membranes (Basel) 3:389–405
61. Ismail AM, Mohammed MI, Fouad SS (2018) Optical and structural properties of polyvinylidene fluoride (PVDF) / reduced graphene oxide (RGO) nanocomposites. J Mol Struct 1170:51–59
62. Al-Saygh A, Ponnamma D, AlMaadeed MAA et al (2017) Flexible pressure sensor based on PVDF nanocomposites containing reduced graphene oxide-titania hybrid nanolayers. Polymers (Basel) 9:33
63. Zhang H, Zhu Y, Li L (2020) Fabrication of PVDF/graphene composites with enhanced β phase: Via conventional melt processing assisted by solid state shear milling technology. RSC Adv 10:3391–3401
64. Pickford T, Gu X, Heeley EL, Wan C (2019) Effects of an ionic liquid and processing conditions on the β-polymorph crystal formation in poly(vinylidene fluoride). CrystEngComm 21:5418–5428
65. Martins P, Lopes AC, Lanceros-Mendez S (2014) Electroactive phases of poly(vinylidene fluoride): Determination, processing and applications. Prog Polym Sci 39:683–706
66. Chhetri S, Kuila T, Murmu NC (2016) In: Nazarpour S (ed) Graphene Technology: From Laboratory to Fabrication. 1st edn. Wiley-VCH, Germany
67. Islam A, Khan AN, Shakir MF, Islam K (2019) Strengthening of β polymorph in PVDF/FLG and PVDF/GO nanocomposites. Mater Res Express 7:15017
68. Zhao X, Zhang Q, Chen D, Lu P (2010) Enhanced mechanical properties of graphene-based polyvinyl alcohol composites. Macromolecules 43:2357–2363

69. Han JK, Jeon DH, Cho SY et al (2016) Nanogenerators consisting of direct-grown piezoelectrics on multi-walled carbon nanotubes using flexoelectric effects. Sci Rep 6:1–8
70. Gebrekrstos A, Madras G, Bose S (2018) Piezoelectric response in electrospun poly(vinylidene fluoride) fibers containing fluoro-doped graphene derivatives. ACS Omega 3:5317–5326
71. Ico G, Showalter A, Bosze W et al (2016) Size-dependent piezoelectric and mechanical properties of electrospun P(VDF-TrFE) nanofibers for enhanced energy harvesting. J Mater Chem A 4:2293–2304
72. Karan SK, Mandal D, Khatua BB (2015) Self-powered flexible Fe-doped RGO/PVDF nanocomposite: An excellent material for a piezoelectric energy harvester. Nanoscale 7:10655–10666
73. Sharma M, Srinivas V, Madras G, Bose S (2016) Outstanding dielectric constant and piezoelectric coefficient in electrospun nanofiber mats of PVDF containing silver decorated multiwall carbon nanotubes: Assessing through piezoresponse force microscopy. RSC Adv 6:6251–6258
74. Singh HH, Singh S, Khare N (2017) Design of flexible PVDF/$NaNbO_3$/RGO nanogenerator and understanding the role of nanofillers in the output voltage signal. Compos Sci Technol 149:127–133
75. Zhang C, Fan Y, Li H et al (2018) Fully Rollable Lead-Free Poly(vinylidene fluoride)-Niobate-Based Nanogenerator with Ultra-Flexible Nano-Network Electrodes. ACS Nano 12:4803–4811
76. Shetty S, Ekbote GS, Mahendran A, Anandhan S (2019) Polymorphism, dielectric and piezoelectric response of organo-modified Ni–Co layered double hydroxide nanosheets dispersed electrospun PVDF nanofabrics. J Mater Sci Mater Electron 30:20703–20715

Publisher's Note Springer Nature remains neutral with regard to jurisdictional claims in published maps and institutional aff iliations.

Journal of Polymer Research is a copyright of Springer, 2021. All Rights Reserved.